# Variable stars in the bulge globular cluster NGC 6401

Y. Tsapras,[1,2]★ A. Arellano Ferro,[3]★ D. M. Bramich,[4] R. Figuera Jaimes,[5,6] N. Kains,[7] R. Street,[2] M. Hundertmark,[6,8] K. Horne,[6] M. Dominik[6] and C. Snodgrass[9,10]

[1]*Astronomisches Rechen-Institut, Zentrum für Astronomie der Universität Heidelberg (ZAH), D-69120 Heidelberg, Germany*
[2]*Las Cumbres Observatory Global Telescope Network, 6740 Cortona Drive, suite 102, Goleta, CA 93117, USA*
[3]*Instituto de Astronomía, Universidad Nacional Autónoma de México. Ciudad Universitaria CP 04510, Mexico*
[4]*Qatar Environment and Energy Research Institute(QEERI), HBKU, Qatar Foundation, Doha, Qatar*
[5]*European Southern Observatory, Karl-Schwarzschild-Straße 2, D-85748 Garching bei München, Germany*
[6]*SUPA, School of Physics and Astronomy, University of St. Andrews, North Haugh, St Andrews KY16 9SS, UK*
[7]*Space Telescope Institute, 3700 San Martin Drive, Baltimore, MD 21218, USA*
[8]*Niels Bohr Institute & Centre for Star and Planet Formation, University of Copenhagen, Øster Voldgade 5, DK-1350 - Copenhagen K, Denmark*
[9]*Planetary and Space Sciences, Department of Physical Sciences, The Open University, Milton Keynes MK7 6AA, UK*
[10]*Max Planck Institute for Solar system Research, Max-Planck-Str. 2, D-37191 Katlenburg-Lindau, Germany*

## ABSTRACT

We present a study of variable stars in globular cluster NGC 6401. The cluster is only $5°.3$ away from the Galactic Centre and suffers from strong differential reddening. The photometric precision afforded us by difference image analysis resulted in improved sensitivity to variability in formerly inaccessible interior regions of the cluster. We find 23 RRab and 11 RRc stars within one cluster radius (2.4 arcmin), for which we provide coordinates, finder-charts and time series photometry. Through Fourier decomposition of the RR Lyrae star light curves we derive a mean metallicity of $[Fe/H]_{UVES} = -1.13 \pm 0.06$ ($[Fe/H]_{ZW} = -1.25 \pm 0.06$), and a distance of $d \approx 6.35 \pm 0.81$ kpc. Using the RR Lyrae population, we also determine that NGC 6401 is an Oosterhoff type I cluster.

**Key words:** stars: variables: RR Lyrae – globular clusters: individual: NGC 6401.

## 1 INTRODUCTION

Globular clusters are gravitationally bound stellar systems which, for the most part, contain between $10^5$ and $10^6$ stars in a volume spanning a few hundred parsecs. These systems are home to some of the oldest stellar populations in the Galaxy and are rich in variable stars of the RR Lyrae type, which are particularly useful for obtaining distance measurements. There are currently 158 globular clusters associated with the Milky Way for which there exist estimates of their distance, metallicity, age and dynamical parameters (Harris 1996).

This paper belongs to a series of studies of variable stars in globular clusters (e.g. Bramich et al. 2011; Arellano Ferro et al. 2013; Figuera Jaimes et al. 2013; Arellano Ferro et al. 2015; Kains et al. 2015) aimed primarily at Fourier decomposing the light curves of RR Lyrae stars in search of physical parameters and at updating the variability census using modern instruments and photometric reduction methods. In particular, the combination of modern CCDs

and the technique of difference image analysis (DIA; Alard & Lupton 1998; Bramich 2008) allows us to probe for variability closer to the crowded central regions of the clusters than was previously possible.

Globular cluster NGC 6401 (also known as GCL1735−238 and ESO520-SC11) is located at equatorial coordinates $(\alpha, \delta)_{J2000} = (17^h38^m37^s, -23°54'32')$ and galactic coordinates $(l, b) = (3°.45, +3°.98)$, only $5°.3$ from the Galactic Centre. According to the 2010 update to the Harris (1996) catalogue, it is a relatively metal-rich cluster ($[Fe/H] \approx -1.02$ dex) with an estimated distance from the Sun of $d_⊙ \approx 10.6$ kpc. However, the metallicity estimate is contradicted by studies done by Davidge (2001) and Valenti, Ferraro & Origlia (2007), who derive metallicities of $[Fe/H] \approx -1.5$ and $[Fe/H] \approx -1.37$ dex, respectively. They conclude that the cluster appears to be metal poor.

The paper is structured as follows. In Section 2, we give an account of our observations and data reduction methods. Section 3 contains a description of our methodological approach to identifying and classifying variable sources in the vicinity of NGC 6401. In Section 4 we provide an account of the Fourier decomposition of the light curves of the RR Lyrae stars and how the derived parameters are used to estimate the physical properties of the cluster. We comment on our results in Section 5 and conclude in Section 6.

★ E-mail: ytsapras@ari.uni-heidelberg.de (YT); armando@astro.unam.mx (AAF)

**Table 1.** The distribution of observations of NGC 6401 for each filter, where the columns $N_g$ and $N_i$ represent the number of images taken in the SDSS-$g'$ and SDSS-$i'$ bands, respectively. We also provide the exposure time(s) employed during each night for each filter in the columns $t_g$ and $t_i$.

| Date | $N_g$ | $t_g$ (s) | $N_i$ | $t_i$ (s) |
|---|---|---|---|---|
| 2013-07-05 | – | – | 2 | 200 |
| 2013-07-07 | – | – | 8 | 200 |
| 2013-07-08 | – | – | 7 | 200 |
| 2013-07-11 | – | – | 4 | 200 |
| 2013-07-12 | – | – | 1 | 200 |
| 2013-07-17 | – | – | 4 | 200 |
| 2013-07-21 | 41 | 60–200 | 48 | 60–200 |
| 2013-07-22 | 8 | 60–200 | 4 | 60 |
| 2013-07-24 | 21 | 60–200 | 29 | 60–200 |
| 2013-07-25 | 39 | 60–200 | 41 | 60–200 |
| 2013-07-26 | 34 | 60–200 | 22 | 60–200 |
| 2013-07-27 | 40 | 60–200 | 43 | 60–200 |
| 2013-07-28 | 13 | 60–200 | 39 | 60–200 |
| 2013-07-29 | 22 | 60–200 | 39 | 60–200 |
| 2013-07-30 | 19 | 60–200 | 18 | 60–200 |
| 2013-07-31 | 25 | 60–200 | 27 | 60–200 |
| 2013-08-01 | 27 | 60–200 | 32 | 60–200 |
| 2013-08-02 | 9 | 60–200 | 12 | 60–200 |
| 2013-08-03 | 22 | 60–200 | 10 | 60–200 |
| 2013-08-04 | 22 | 60–200 | 18 | 60–200 |
| 2013-08-05 | 14 | 60–200 | 20 | 60–200 |
| 2013-08-08 | 2 | 60 | 4 | 60–200 |
| 2013-08-09 | 39 | 60–200 | 36 | 60–200 |
| 2013-08-10 | 16 | 60–200 | 23 | 60–200 |
| 2013-08-11 | 12 | 60–200 | 18 | 60–200 |
| Total: | 425 | | 509 | |

## 2 OBSERVATIONS AND REDUCTIONS

### 2.1 Observations

Observations of the target field were a by-product of the RoboNet microlensing campaign (Tsapras et al. 2009) and were obtained in the campaign-specific SDSS-$g'$ and SDSS-$i'$ bands throughout the months of 2013 July and August using the LCOGT[1] 1-m robotic telescope network. The LCOGT telescopes are clones of each other, featuring identical instruments, and are deployed in clusters of two to three at the Siding Spring Observatory (SSO), South African Astronomical Observatory (SAAO) and Cerro Tololo Inter-American Observatory (CTIO). The detectors used were standard SBIG STX-16803, with $4096 \times 4096$ pixels, each 0.23 arcsec, giving a field of view of $15.8 \times 15.8$ arcmin$^2$. Image binning was set to $2 \times 2$, giving an effective pixel scale of 0.47 arcsec. A summary of the observations can be found in Table 1.

### 2.2 Difference image analysis

Using our DANDIA[2] pipeline (Bramich et al. 2013), we performed DIA on the images to extract high-precision photometric measurements. Since all images were obtained from a network of identical telescopes, all images taken with the same filter were processed together, regardless of which telescope they originated from.

---

At the first step, every image underwent standard debiasing and flat-fielding calibrations. Subsequently, a reference (template) image was constructed for each filter by combining a set of registered best-seeing images obtained with the same instrument. For each reference image we measured the fluxes and positions of all point spread function (PSF)-like objects (stars) by extracting a spatially variable empirical PSF from the image and fitting this PSF to each detected object. Image registration was performed using the triangle matching method of Pal & Bakos (2006) to match the stars detected in each image with those detected in the reference, and then deriving a linear transformation between the images that uses cubic O-MOMS resampling (Blu, Thevenaz & Unser 2001). In this way, all images were geometrically aligned to match the relevant reference.

Difference images were generated by subtracting the relevant reference image, convolved with an appropriate spatially variable kernel, from each registered image. The spatially variable convolution kernel was determined using bilinear interpolation of a set of kernels, modelled as discrete pixel arrays (Bramich 2008), that were derived for a uniform $13 \times 13$ grid of subregions across the image.

Difference fluxes for each star detected in the reference image were evaluated from each difference image by using fixed position PSF photometry. Light curves were constructed by calculating the total flux $f_{tot}(t)$ in ADU/s at each epoch $t$ using:

$$f_{tot}(t) = f_{ref} + \frac{f_{diff}(t)}{p(t)} \tag{1}$$

where $f_{ref}$ is the reference flux (ADU/s), $f_{diff}(t)$ is the differential flux (ADU/s) and $p(t)$ is the photometric scale factor (the integral of the kernel solution).

To convert to instrumental magnitudes, we used

$$m_{ins}(t) = 25.0 - 2.5 \log[f_{tot}(t)] \tag{2}$$

where $m_{ins}(t)$ is the instrumental magnitude of the star at time $t$. Uncertainties were propagated in the appropriate analytical fashion.

The above procedure and its caveats have been described in detail in Bramich et al. (2011) and the interested reader is referred to the paper for relevant details.

### 2.3 Photometric calibrations

#### 2.3.1 Relative

Systematic errors in photometric measurements are caused by a whole range of effects such as mismatches between the true and measured flat-field calibrations, insufficiently accurate modelling of the spatially varying PSF, poor image subtractions in DIA, etc. These types of errors affect all light curves to a greater or lesser extent depending on the data properties and photometry algorithms employed. Although it is not possible to suppress them completely, it is often the case that substantial qualitative improvements can be made when dealing with time series photometry (e.g. Bramich et al. 2015; Kains et al. 2015). We used the method from Bramich & Freudling (2012) to determine the magnitude offsets $Z_k$ that should be applied to each photometric measurement from the image $k$, which translates into a correction for any systematic errors introduced into the DIA photometry due to errors in the fitted photometric scale factors $p(t)$. The offsets derived were of the order of $\sim$1–2 per cent for the SDSS-$g'$ band, and somewhat smaller for the SDSS-$i'$ band. The application of this correction substantially improved the quality of the light curves.
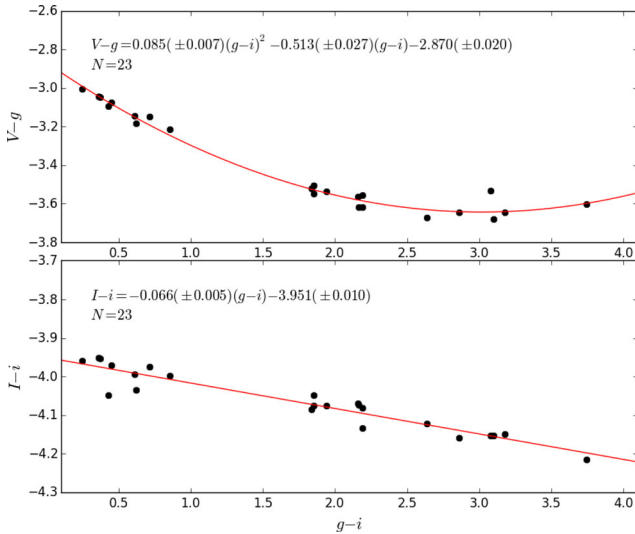
**Figure 1.** Transformation relations between the instrumental and the standard photometric systems using a set of standard stars in the field of NGC 6401 provided by Peter Stetson.

### 2.3.2 Absolute

We identified 23 standard stars in the field of NGC 6401 from the online collection of Stetson (2000)[3] which we used to transform instrumental $(g, i)$ magnitudes into the standard $(V, I)$ system. Our derived transformations are depicted in Fig. 1. For the $i$ band we obtained a linear relation, as expected, since the SDSS-$i'$ band is similar to the Johnson–Cousins $I$ band. However, for the observations in the $g$ band, we obtained a non-linear (quadratic) relation. This is due to the fact that the SDSS-$g'$ band is bluer than the Johnson–Cousins $V$-band (Ivezic et al. 2007). Furthermore, NCG 6401 is heavily affected by differential reddening which is more evident in the bluer bands. The analytical transformations used for the calibration are as follows:

$$V_{\text{std}} = g + 0.085(\pm 0.007)(g - i)^2 - 0.513(\pm 0.027)(g - i)$$
$$- 2.870(\pm 0.020), \qquad (3)$$

$$I_{\text{std}} = i - 0.066(\pm 0.005)(g - i) - 3.951(\pm 0.010). \qquad (4)$$

It is important to note that while these transformations shift the instrumental magnitudes to the $V$ and $I$ magnitude scales, the fact that the photometry pertains to the $g$ and $i$ bands remains unchanged. Hence the transformations do not affect the overall shape/amplitude of the light curves for the variable stars in our sample, and the light curves we present are simply $g$- and $i$-band light curves on the standard $V$ and $I$ brightness scale.

Once these transformations were applied to the light curves, we proceeded to generate the colour–magnitude diagram (CMD) shown in Fig. 2 using the inverse-variance-weighted mean $V$ and $I$ magnitudes for 23 698 stars identified in our images. Blue and green filled circles mark the relevant locations on the diagram for the cluster RRab and RRc stars, respectively (see Section 3). The plot shows an almost vertical main sequence (MS) between magnitudes 15 and 20, which is mostly due to contamination from foreground stars in
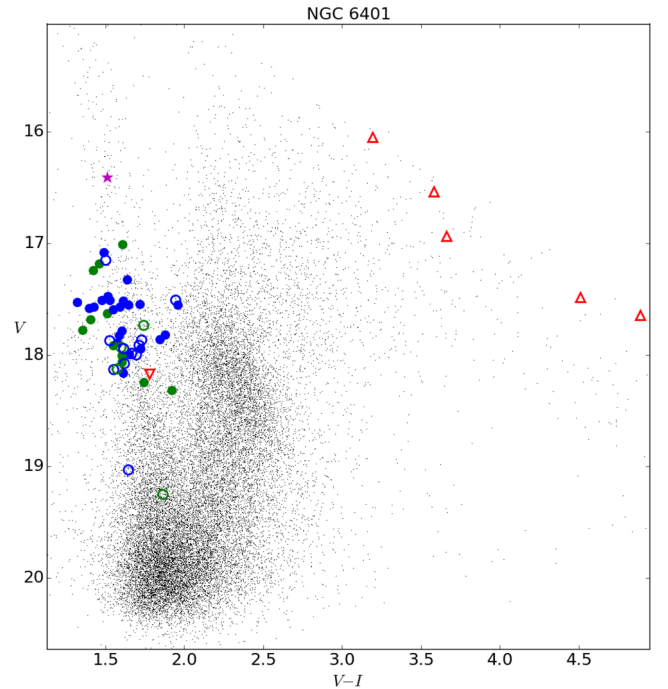
**Figure 2.** CMD of NGC 6401. Blue and green filled circles mark the cluster RRab and RRc stars, respectively. Unfilled circles represent non-cluster RR Lyraes. The triangles on the top right are LPVs NSV09307, NSV09288, LPV9, LPV10 and LPV11. The purple star marks the location of V3. The inverted red triangle on the middle-left of the plot ($V \sim 18.1$) is variable E1.

the Galactic disc. The red horizontal branch (RHB) is the concentration of stars at $V \sim 18$, which is mixed with the fainter end of the red giant branch (RGB). The tilted RGB extends to magnitude $V - I \sim 5$–6. Some differential reddening is present, indicated by the tilt and elongation of the RHB and RGB.

To validate the transformations, we compare our calibrated magnitudes with a set of 1041 photometrically calibrated OGLE stars from the field BLG626.24 in the vicinity of NGC 6401[4] and find that for the majority of these stars the magnitudes match to within $\sim 0.06$ mag. Calibrated photometry for all the variables identified in this work can be found in Table 2.

### 2.4 Astrometry

We used the GAIA (Draper et al. 2000) image display tools to derive a linear astrometric solution for the SDSS-$g'$ filter reference image by matching 1429 stars from the UCAC4 star catalogue (Zacharias 2012). After manually rejecting saturated stars and stars at the edges of the image we achieved a radial rms scatter in the residuals of $\sim 0.22$ arcsec. Similarly, for the SDSS-$i'$ filter we used 1528 stars from the UCAC4 catalogue and obtained an rms of $\sim 0.25$ arcsec. The astrometric fit was then used to calculate the J2000.0 celestial coordinates for all of the confirmed variables in our field of view (see Tables 3 and 4).

## 3 VARIABLE STARS IN NGC 6401

A series of searches for variable stars at and around NGC 6401 conducted in the 1970s by Terzan & Rutily (1972, 1973, 1975) yielded

**Table 2.** Time-series SDSS-$g'$ and SDSS-$i'$ photometry, linearly transformed to the $V$ and $I$ bands, respectively, for all of the confirmed variables in our field of view. The standard $M_{std}$ and instrumental $m_{ins}$ magnitudes are listed in Columns 4 and 5, respectively, corresponding to the variable star, filter, and epoch of mid-exposure listed in Columns 1–3, respectively. The uncertainty on $m_{ins}$ is listed in Column 6, which also corresponds to the uncertainty on $M_{std}$. For completeness, we also list the quantities $f_{ref}$, $f_{diff}$ and $p$ from equation (1) in Columns 7, 9 and 11, along with the uncertainties $\sigma_{ref}$ and $\sigma_{diff}$ in Columns 8 and 10. This is an extract from the full table, which is available with the electronic version of the article.

| Variable star ID | Filter | HJD (d) | $M_{std}$ (mag) | $m_{ins}$ (mag) | $\sigma_m$ (mag) | $f_{ref}$ (ADU s$^{-1}$) | $\sigma_{ref}$ (ADU s$^{-1}$) | $f_{diff}$ (ADU s$^{-1}$) | $\sigma_{diff}$ (ADU s$^{-1}$) | $p$ |
|---|---|---|---|---|---|---|---|---|---|---|
| V2 | g | 2456495.20657 | 18.024 | 21.286 | 0.145 | 34.473 | 0.924 | −6.838 | 7.218 | 1.7640 |
| V2 | g | 2456495.21746 | 17.956 | 21.218 | 0.110 | 34.473 | 0.924 | −3.424 | 5.963 | 1.8019 |
| ⋮ | ⋮ | ⋮ | ⋮ | ⋮ | ⋮ | ⋮ | ⋮ | ⋮ | ⋮ | ⋮ |
| V2 | i | 2456479.64343 | 16.088 | 20.099 | 0.011 | 103.089 | 2.051 | −24.881 | 1.968 | 2.1117 |
| V2 | i | 2456479.74302 | 16.186 | 20.196 | 0.020 | 103.089 | 2.051 | −12.404 | 0.994 | 0.6315 |
| ⋮ | ⋮ | ⋮ | ⋮ | ⋮ | ⋮ | ⋮ | ⋮ | ⋮ | ⋮ | ⋮ |

**Table 3.** Details for all confirmed RR Lyrae stars within one cluster radius (2.4 arcmin) from the NGC 6401 cluster centre. Period estimates for each variable from this work are reported in Column 4 and from previous studies in Column 5 for comparison. Mean magnitudes are reported in Columns 8 and 9 and peak-to-peak amplitudes in Columns 10 and 11. The epoch reported in Column 12 is the light-curve maximum.

| Variable star ID | OGLE ID | Variable type | Period (d) | OGLE period (d) | RA (J2000.0) | Dec (J2000.0) | $\langle V \rangle$ (mag) | $\langle I \rangle$ (mag) | $A_g$ (mag) | $A_i$ (mag) | Epoch (HJD-2450000) |
|---|---|---|---|---|---|---|---|---|---|---|---|
| V2 | OGLE-BLG-RRLYR-24004 | RRab | 0.70158 | 0.70235 | 17:38:33.97 | −23:54:26.6 | 17.66 | 15.94 | 0.93 | 0.48 | 6500.9323 |
| V4 | OGLE-BLG-RRLYR-24049 | RRab | 0.47233 | 0.47248 | 17:38:36.36 | −23:54:35.2 | – | – | 1.18 | – | 6499.2669 |
| V5 | OGLE-BLG-RRLYR-24006 | RRab | 0.53289 | 0.53386 | 17:38:34.01 | −23:54:40.8 | 18.23 | 16.39 | 1.19 | 0.64 | 6514.9621 |
| V6 | OGLE-BLG-RRLYR-24078 | RRab | 0.44446 | 0.44417 | 17:38:38.19 | −23:53:58.2 | 17.96 | 16.37 | 1.55 | 0.91 | 6507.3248 |
| V7 | OGLE-BLG-RRLYR-24126 | RRab | 0.54563 | 0.54575 | 17:38:40.99 | −23:54:32.3 | 17.60 | 16.00 | 1.19 | 0.62 | 6495.2935 |
| V8 | – | RRc | 0.32485 | – | 17:38:38.72 | −23:55:25.0 | 17.71 | 16.13 | 0.54 | 0.24 | 6508.3582 |
| V9 | OGLE-BLG-RRLYR-24055 | RRab | 0.51367 | 0.51311 | 17:38:36.76 | −23:54:39.2 | 17.51 | 15.75 | 1.15 | 0.54 | 6505.9660 |
| V10 | – | RRab | 0.52603 | – | 17:38:38.57 | −23:53:52.4 | 17.88 | 16.20 | 1.32 | 0.68 | 6503.5181 |
| V11 | OGLE-BLG-RRLYR-24121 | RRab | 0.58212 | 0.58183 | 17:38:40.82 | −23:54:08.2 | 17.59 | 16.00 | 0.90 | 0.46 | 6501.5939 |
| V12 | OGLE-BLG-RRLYR-24030 | RRc | 0.29130 | 0.29109 | 17:38:35.09 | −23:54:30.8 | 17.23 | 15.73 | 0.67 | 0.34 | 6503.5043 |
| V13 | OGLE-BLG-RRLYR-24036 | RRab | 0.56498 | 0.56527 | 17:38:35.63 | −23:54:49.0 | 18.04 | 16.31 | 1.13 | 0.59 | 6495.4983 |
| V14 | – | RRab | 0.60851 | – | 17:38:39.37 | −23:54:39.0 | 17.58 | 15.84 | 0.54 | 0.24 | 6495.3499 |
| V15 | OGLE-BLG-RRLYR-24075 | RRab | 0.50440 | 0.50644 | 17:38:37.78 | −23:55:09.5 | 17.84 | 16.21 | 1.30 | 0.71 | 6499.2100 |
| V16 | OGLE-BLG-RRLYR-24043 | RRab | 0.50581 | 0.50552 | 17:38:36.00 | −23:55:58.1 | 18.51 | 16.63 | 1.27 | 0.70 | 6505.5065 |
| V17 | OGLE-BLG-RRLYR-24131 | RRab | 0.50517 | 0.50524 | 17:38:41.67 | −23:52:57.0 | 17.22 | 15.62 | 1.34 | 0.74 | 6501.7732 |
| V18 | OGLE-BLG-RRLYR-24002 | RRab | 0.56830 | 0.57021 | 17:38:33.84 | −23:54:03.8 | 17.71 | 16.05 | 1.25 | 0.66 | 6499.5121 |
| V19 | OGLE-BLG-RRLYR-24160 | RRab | 0.55989 | 0.55949 | 17:38:43.80 | −23:56:12.1 | 17.63 | 16.04 | 1.06 | 0.57 | 6507.4949 |
| V21 | OGLE-BLG-RRLYR-24056 | RRc | 0.27809 | 0.27814 | 17:38:36.77 | −23:54:12.2 | 17.86 | 16.46 | 0.52 | 0.30 | 6507.9500 |
| V22 | OGLE-BLG-RRLYR-24025 | RRc | 0.29972 | 0.29971 | 17:38:34.87 | −23:54:40.6 | 17.98 | 16.37 | 0.50 | 0.24 | 6499.2900 |
| V23 | OGLE-BLG-RRLYR-24100 | RRc | 0.36641 | 0.36647 | 17:38:39.91 | −23:52:27.2 | 17.28 | 15.82 | 0.51 | 0.25 | 6501.0665 |
| V24 | OGLE-BLG-RRLYR-24182 | RRab | 0.52000 | 0.52013 | 17:38:45.53 | −23:53:54.8 | 17.65 | 16.01 | 1.05 | 0.55 | 6507.9216 |
| V25 | OGLE-BLG-RRLYR-24047 | RRab | 0.55867 | 0.55860 | 17:38:36.27 | −23:55:03.0 | 17.55 | 15.59 | 0.71 | 0.28 | 6504.6719 |
| V26 | OGLE-BLG-RRLYR-23926 | RRab | 0.49585 | 0.49683 | 17:38:28.16 | −23:54:24.2 | 18.22 | 16.33 | 1.16 | 0.59 | 6509.9683 |
| V27 | OGLE-BLG-RRLYR-23985 | RRc | 0.28743 | 0.28783 | 17:38:33.01 | −23:55:04.8 | 18.40 | 16.40 | 0.55 | 0.19 | 6503.4900 |
| V28 | OGLE-BLG-RRLYR-23999 | RRab | 0.62576 | 0.62373 | 17:38:33.56 | −23:56:52.8 | 18.00 | 16.24 | 0.54 | 0.34 | 6499.5121 |
| V29 | OGLE-BLG-RRLYR-24011 | RRc | 0.28860 | 0.28856 | 17:38:34.16 | −23:55:07.2 | 18.34 | 16.52 | 0.55 | 0.24 | 6503.0370 |
| V30 | OGLE-BLG-RRLYR-24021 | RRc | 0.26198 | 0.26207 | 17:38:34.79 | −23:55:05.0 | 18.07 | 16.42 | 0.42 | 0.20 | 6498.4785 |
| V31 | OGLE-BLG-RRLYR-24024 | RRab | 0.57712 | 0.57840 | 17:38:34.87 | −23:54:35.6 | 18.00 | 16.06 | 0.91 | 0.39 | 6495.4983 |
| V32 | OGLE-BLG-RRLYR-24037 | RRab | 0.66136 | 0.66059 | 17:38:35.65 | −23:54:51.8 | 17.94 | 15.96 | 0.68 | 0.30 | 6495.2728 |
| V33 | OGLE-BLG-RRLYR-24039 | RRc | 0.34032 | 0.34087 | 17:38:35.70 | −23:55:26.3 | 18.13 | 16.48 | 0.50 | 0.25 | 6503.6545 |
| V34 | OGLE-BLG-RRLYR-24060 | RRab | 0.54441 | 0.54533 | 17:38:36.79 | −23:54:35.4 | 17.60 | 15.93 | 0.90 | 0.41 | 6505.6228 |
| V35 | OGLE-BLG-RRLYR-24062 | RRc | 0.28284 | 0.28300 | 17:38:37.00 | −23:54:35.5 | 17.05 | 15.41 | 0.31 | 0.12 | 6501.6900 |
| V36 | OGLE-BLG-RRLYR-24142 | RRc | 0.31898 | 0.31905 | 17:38:42.86 | −23:52:57.3 | 17.76 | 16.29 | 0.44 | 0.23 | 6500.5692 |
| V37 | OGLE-BLG-RRLYR-24148 | RRab | 0.47915 | 0.47961 | 17:38:43.06 | −23:52:35.3 | 17.93 | 16.23 | 1.38 | 0.77 | 6500.0600 |

**Table 4.** Details for all remaining confirmed variables in the field of NGC 6401. Period estimates for each variable from this work are reported in Column 3 and from previous studies in Column 4 for comparison. Mean magnitudes are reported in Columns 7 and 8. The epoch reported in Column 9 is the light-curve maximum.

| Variable star ID | Variable type | Period (d) | OGLE period (d) | RA (J2000.0) | Dec. (J2000.0) | $\langle V \rangle$ (mag) | $\langle I \rangle$ (mag) | Epoch (HJD-2450000) |
|---|---|---|---|---|---|---|---|---|
| V3 | CWB | 1.74869 | – | 17:38:41.31 | −23:54:34.9 | 16.41 | 14.90 | 6497.9440 |
| E1 | EB | 1.33228 | – | 17:38:37.42 | −24:00:52.0 | 18.17 | 16.39 | 6495.4922 |
| LPV1 | LPV | – | – | 17:38:41.02 | −23:56:26.6 | – | – | 6495.4983 |
| LPV2 | LPV | – | – | 17:38:36.89 | −23:49:23.5 | – | – | 6509.6726 |
| LPV3 | LPV | – | – | 17:38:36.35 | −23:54:20.5 | – | – | 6509.2758 |
| LPV4 | LPV | – | – | 17:38:33.28 | −23:58:37.9 | – | – | 6498.5154 |
| LPV5 | LPV | – | – | 17:38:31.02 | −23:48:47.8 | – | – | 6501.7620 |
| LPV6 | LPV | – | – | 17:38:29.84 | −23:57:17.1 | – | – | 6503.5181 |
| LPV7 | LPV | – | – | 17:38:23.66 | −23:51:26.8 | – | – | 6507.5209 |
| LPV8 | LPV | – | – | 17:38:18.85 | −23:51:04.2 | – | – | 6501.7620 |
| LPV9 | LPV | – | – | 17:38:15.93 | −24:00:04.6 | 16.54 | 12.96 | 6514.6812 |
| LPV10 | LPV | – | – | 17:38:12.37 | −23:51:55.4 | 16.93 | 13.27 | 6516.5155 |
| LPV11 | LPV | – | – | 17:38:08.05 | −23:47:16.6 | 16.04 | 12.85 | 6514.4772 |
| LPV12 | LPV | – | – | 17:38:41.74 | −23:54:22.4 | – | – | 6495.2174 |
| NSV 09288 | LPV | – | – | 17:38:02.73 | −23:46:41.4 | 17.48 | 12.97 | 6514.4762 |
| NSV 09307 | LPV | – | – | 17:38:17.70 | −24:01:29.9 | 17.65 | 12.75 | 6495.5296 |
| NSV 09349 | LPV | – | – | 17:38:46.09 | −23:47:33.3 | – | – | 6503.5034 |
| V2226 Oph | LPV | – | – | 17:38:21.23 | −23:50:43.7 | – | – | 6503.5181 |
| V2227 Oph | LPV | – | – | 17:38:21.80 | −23:55:22.7 | – | – | 6516.5146 |
| OGLE-BLG-RRLYR-23731 | RRab | 0.68325 | 0.68279 | 17:38:09.55 | −24:01:35.9 | 17.87 | 16.34 | 6495.2390 |
| OGLE-BLG-RRLYR-23799 | RRab | 0.52350 | 0.52347 | 17:38:16.60 | −23:46:36.7 | – | – | 6495.3700 |
| OGLE-BLG-RRLYR-23863 | RRab? | 0.68212 | 0.68160 | 17:38:22.97 | −23:51:51.6 | 17.74 | 16.00 | 6498.5800 |
| OGLE-BLG-RRLYR-23880 | RRab | 0.55167 | 0.55149 | 17:38:24.43 | −23:51:49.2 | 17.98 | 16.32 | 6495.7350 |
| OGLE-BLG-RRLYR-23969 | RRc | 0.32692 | 0.32682 | 17:38:31.63 | −23:50:06.4 | 19.27 | 17.40 | 6495.8150 |
| OGLE-BLG-RRLYR-24007 | RRab | 0.44022 | 0.43985 | 17:38:34.08 | −23:59:28.3 | 19.03 | 17.38 | 6497.4737 |
| OGLE-BLG-RRLYR-24026 | RRab | 0.50640 | 0.50689 | 17:38:34.89 | −23:57:13.5 | 17.99 | 16.33 | 6495.1150 |
| OGLE-BLG-RRLYR-24044 | RRab | 0.46785 | 0.46743 | 17:38:36.09 | −23:50:17.5 | 18.02 | 16.30 | 6509.9880 |
| OGLE-BLG-RRLYR-24050 | RRc | 0.36286 | 0.36284 | 17:38:36.46 | −24:01:15.3 | 18.12 | 16.55 | 6501.9897 |
| OGLE-BLG-RRLYR-24058 | RRab | 0.60849 | 0.60920 | 17:38:36.79 | −23:51:51.3 | 17.87 | 16.14 | 6500.7392 |
| OGLE-BLG-RRLYR-24066 | RRab | 0.51589 | 0.51623 | 17:38:37.43 | −23:47:53.4 | – | – | 6500.6292 |
| OGLE-BLG-RRLYR-24124 | RRab | 0.49729 | 0.49800 | 17:38:40.86 | −23:51:59.3 | 17.15 | 15.66 | 6509.0082 |
| OGLE-BLG-RRLYR-24138 | RRc | 0.31636 | 0.31635 | 17:38:42.60 | −24:01:22.4 | 17.93 | 16.34 | 6507.7153 |
| OGLE-BLG-RRLYR-24255 | RRab | 0.61989 | 0.61915 | 17:38:50.64 | −23:54:11.7 | 17.51 | 15.57 | 6496.2955 |
| OGLE-BLG-RRLYR-24293 | RRab | 0.53190 | 0.53177 | 17:38:53.97 | −23:53:30.3 | 18.07 | 16.45 | 6496.2615 |
| OGLE-BLG-RRLYR-24325 | RRab | 0.51808 | 0.51817 | 17:38:56.67 | −23:56:19.0 | 18.13 | 16.58 | 6499.2784 |
| OGLE-BLG-RRLYR-24383 | RRab | 0.61407 | 0.61420 | 17:39:02.24 | −24:00:54.3 | 17.91 | 16.20 | 6504.9341 |

25 variables (labelled V1–25) that could be cluster members.[5] They are listed in the Clement et al. (2001) catalogue in the 2015 January update.[6] However, detailed studies of these variables were never published.

The first observations of this cluster using CCDs were performed by Barbuy et al. (1999), who observed for a single night (1998 July 4) with the 1.5-m Danish telescope at ESO (La Silla). Although theirs was not a search for variables, they performed PSF-fitting photometry with Daophot II (Stetson 1987) on their images and used their CMD diagrams to estimate the amount of reddening and the cluster's distance from the Sun.

NGC 6401's proximity to the Galactic bulge places it in the fields monitored by the fourth phase of the Optical Gravitational Lensing Experiment (OGLE) survey which started operations in 2011 (Udalski, Szymanski & Szymanski 2015). Soszynski et al. (2014) present a comprehensive collection of ~38000 RR Lyrae stars detected over 182 deg$^2$ monitored by the OGLE-IV survey in the densest regions of the Galactic bulge. Of those, ~300 are identified as plausible members of 15 globular clusters. Their list includes 31 RR Lyrae stars lying within one cluster angular radius from the centre of NGC 6401, several of which were previously unknown. Their photometric reductions were performed using the OGLE real time photometric pipeline (Udalski 2003), which is based on DIA, and the final photometry of selected variables was calibrated to the standard *VI* system with an estimated zero-point accuracy of ~0.02 mag.

### 3.1 Detection of new variable stars

Our pipeline generated 26727 and 31762 light curves for the stars measured in the SDSS-*g*′ and SDSS-*i*′ reference images, respectively. We proceeded by compiling a list of known variables in a 16 × 16 arcmin$^2$ area centred on NGC 6401 using the equatorial

---

[5] They also identified a large number of variable star candidates in our field of view that are not cluster members, but we have not been able to recover any of them in our search.
[6] http://www.astro.utoronto.ca/cclement/cat/C1735m238

coordinates and finding charts available in the OGLE-IV data base[7] and the coordinates provided by Samus at al. (2009a). We also considered long period variables (LPV) in the General Catalog of Variable Stars (GCVS)[8] (Samus et al. 2009b) and the International Variable Star Index (VSX) of the American Association of Variable Star Observers (AAVSO).[9]

In order to identify variable sources in our data, we employed three different methods. Using all SDSS-$g'$ band light curves, we performed a Lomb–Scargle (LS) periodogram search for periods between 0.1 and 1.3 d (method 1), retaining the best-fitting periods. A subsequent second run with no restriction on the period was performed to identify variables that vary on longer time-scales. For the same set of light curves, we also evaluated the $\mathcal{S_B}$ variability statistic (method 2), as defined in equation (3) from Figuera Jaimes et al. (2013). Data points deviating more than three times the rms error from the mean magnitude were clipped during this process. This removed between 0 and 4 data points from the light curves but mostly left them unaffected. Lastly, for each filter we constructed a 'residual superimage' by taking the absolute value of the residual ADU counts at each pixel ($i$, $j$) for every difference image and summing over the images (method 3). For a detailed description of the method, see Bramich et al. (2011). Variable sources were easier to spot with this method since their PSF-like peaks on the superimage were strongly enhanced.

To select candidate variable stars, we required $\mathcal{S_B} > 1.0$ and best-period LS Power score$>0.4$. These selection criteria were decided empirically by looking at the respective distributions of these parameters, and were intentionally set low enough so as to ensure no candidate variables were missed.

Upon visual inspection of the candidates, after removing duplicates and bad quality light curves, 62 were retained as showing genuine variability. Almost all previously known variables were identified by this procedure. However, we did not find any evidence of variability for any of the sources identified in the immediate vicinity of the coordinates of previously reported variables V1, V20, which were also not found in the OGLE variable data base, and OGLE-BLG-RRLYR-23724. We note that the OGLE data base also does not contain any variables in the reported coordinates of V3, V8, V10 and V14, all of which were identified by our analysis.

From the residual superimages in each filter, we selected candidate variables by visually identifying all PSF-like objects. We then examined the light curves corresponding to the coordinates of these objects and identified eight additional variables, bringing the total to 70. Our results are summarized in Tables 3 and 4, which list all of the confirmed variable stars in our field of view.

We found 37 RRab and 14 RRc variables within a 15.8 × 15.8 arcmin$^2$ field centred at the coordinates of NGC 6401. Of these, 23 RRab and 11 RRc are within one cluster radius[10] (2.4 arcmin) from the centre of NGC 6401 and most likely belong to the cluster. Finding charts are provided in Figs 3 and 4. The variable light curves for the likely cluster members are displayed in Figs 5 and 6, and their locations on the CMD are shown in Fig. 2. The light curves of other variables are plotted in Figs A1 and A2.

Cluster variables listed in Table 3 are denoted by the letter V, with all numbers up to 25 belonging to the Terzan & Rutily lists. OGLE

identifiers, where available, are also provided in the second column. Our best-fitting periods and the OGLE periods are given in Columns 4 and 5, respectively. Non-member variables are listed in Table 4, which includes 17 LPV with periods $>27$ d. Their light curves are displayed in the Appendix. LPVs 1 to 12 are new discoveries. We note that the shape of the light curve of variable V3 suggests that it is most likely a W Virginis (CWB) star with a period of ~1.75 d. The eclipsing binary E1 is also a new discovery. All light curves are available for download in the electronic version of this article. An excerpt from the full table of electronic data is provided in Table 2.

### 3.2 The case of variable V12

We detected two independent frequencies in the SDSS-$g'$ and SDSS-$i'$ light curves of the RR Lyrae. The frequency spectra are shown in Fig. 7. The top panels show the prominent peaks, which alternate in intensity between the $g$ band and the $i$-band case. Pre-whitening the strongest peak leads to the spectra shown in the middle panels. In both cases the secondary peak persists, which demonstrates that these signals are not aliases of each other. Subsequent pre-whitening of the secondary peak removes all signals as seen in the bottom panels.

The frequency ratio of these two signals is 0.884, i.e. far from the canonical 0.745 expected if this star was a radial double mode pulsator RR01 (RRd) (fundamental-first overtone) or 0.80 for RR12 stars (first and second overtone modes). No RR12 have yet been identified in globular clusters but three were detected by Alcock et al. (2000) in the Large Magellanic Cloud (LMC). From this we may conclude that in the case of V12 either one or both pulsation modes are non-radial.

Other non-radial pulsators among first overtone or RR1 RR Lyraes have been identified in the globular cluster M55 (Olech et al. 1999) and by Alcock et al. (2000) in the LMC. The fundamental difference of V12 with all these non-radial pulsator RR Lyrae is that in all of them the frequency ratio is always larger than 0.95, whereas it is only 0.884 in V12. Thus V12 adds to the list of non-radial pulsator RR Lyrae stars in globular clusters. Precise determination of the excited non-radial mode would require abundant and accurate data.

## 4 DETERMINATION OF THE PHYSICAL PARAMETERS FROM THE RR LYR VARIABLES

We used Fourier decomposition of the calibrated SDSS-$g'$ and SDSS-$i'$ band RR Lyr light curves into their harmonics in order to estimate the metallicity, luminosity and effective temperature of the stars. Fourier decomposition involves modelling the light curves as a Fourier series of the form:

$$m(t) = A_0 + \sum_{k=1}^{N} A_k \cos\left[\frac{2\pi}{P} k(t - E) + \phi_k\right], \qquad (5)$$

where $m(t)$ is the magnitude at time $t$, $N$ the number of harmonics used in the fit, $P$ the period of variability and $E$ the reference epoch. $A_k$ and $\phi_k$ are the amplitudes and phases of the sinusoidal components, respectively. The fit to the data was performed using linear least squares, and the best-fitting values of the amplitudes and phases of the harmonics were evaluated. From these, the Fourier parameters $\phi_{ij} = j\phi_i - i\phi_j$ and $R_{ij} = A_i/A_j$ were determined. In order to avoid fitting noise in the data, each variable was modelled with
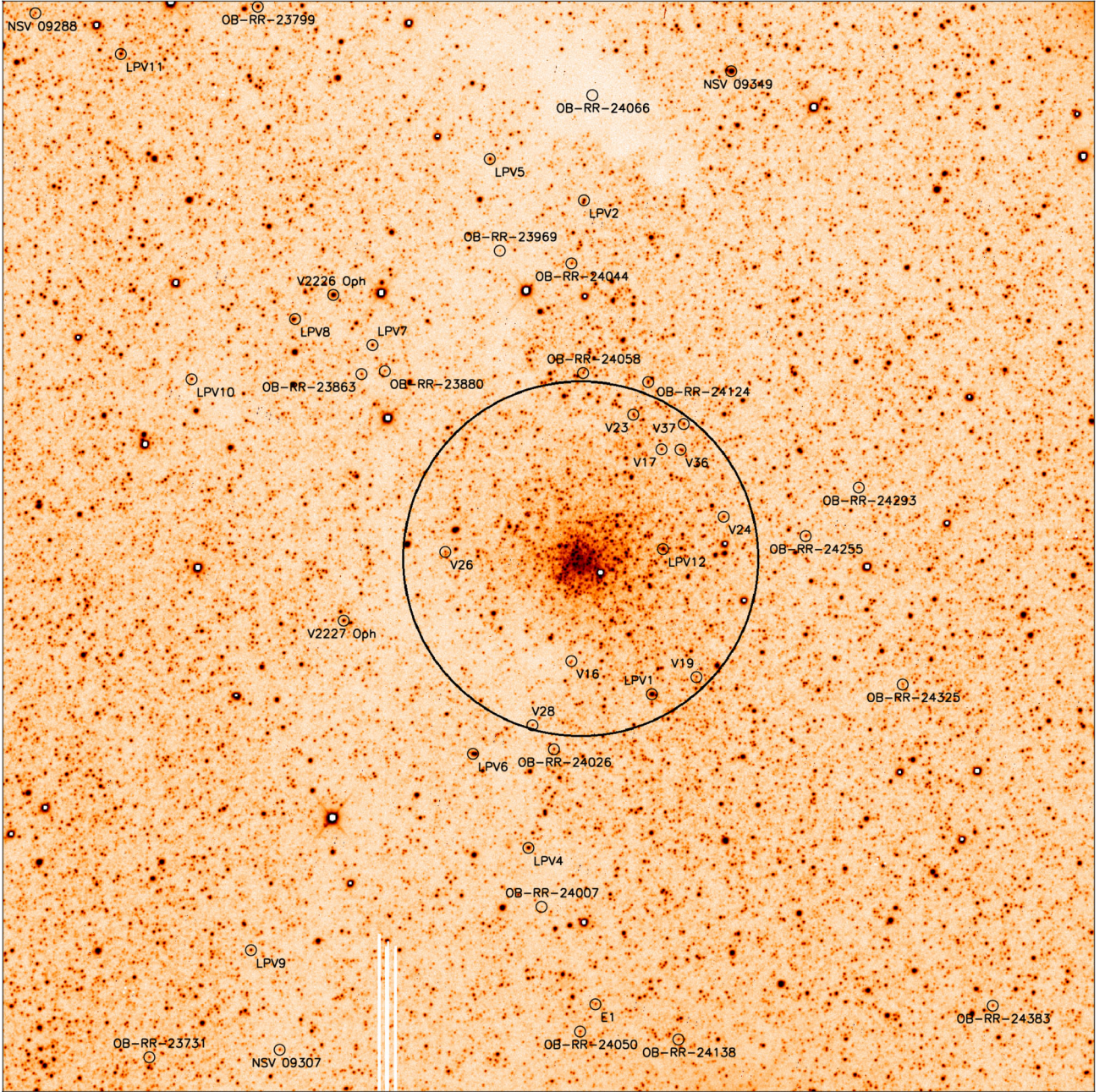
**Figure 3.** Finding chart constructed from our SDSS-$g'$ band reference image. North is up and East is to the right. The cluster image is $15.8 \times 15.8$ arcmin$^2$. All of the confirmed variables in our FoV are identified, except in the crowded cluster core (see Fig. 4). The circle marks the cluster radius of 2.4 arcmin. OGLE variable names have been abbreviated for clarity.

the lowest possible number of harmonics. We note that, where available, we used the OGLE data to refine the estimates of the periods during the fitting process.

Since our observations were originally in the SDSS-$g'$ and SDSS-$i'$ bands, we performed our fits in each band using the alternative Fourier form:

$$m(t) = A_0 + \sum_{k=1}^{N} B_k \cos\left[\frac{2\pi}{P}k(t-E)\right] + C_k \sin\left[\frac{2\pi}{P}k(t-E)\right], \quad (6)$$

from which we derived the coefficients $B_k$ and $C_k$. These Fourier coefficients were then converted to their equivalents in the $V$ band using the Lupton (2005) transformations between SDSS magnitudes and UBVRcIc combined with our equation (4), from which we derived $B_k(V) = 0.5778 B_k(g) + 0.4222 B_k(i)$ and $C_k(V) = 0.5778 C_k(g) + 0.4222 C_k(i)$. We then estimated the coefficients $A_k(V) = \sqrt{B_k(V)^2 + C_k(V)^2}$ and $\phi_k(V) = \cos^{-1}(B_k(V)/A_k(V))$.

The best-fitting parameters and number of harmonics used for individual RRab and RRc variable light curves are listed in Table 5. Some variables did not provide useful constraints and were excluded from further analysis. Specifically, when determining the physical parameters, we did not use the following variables: V12
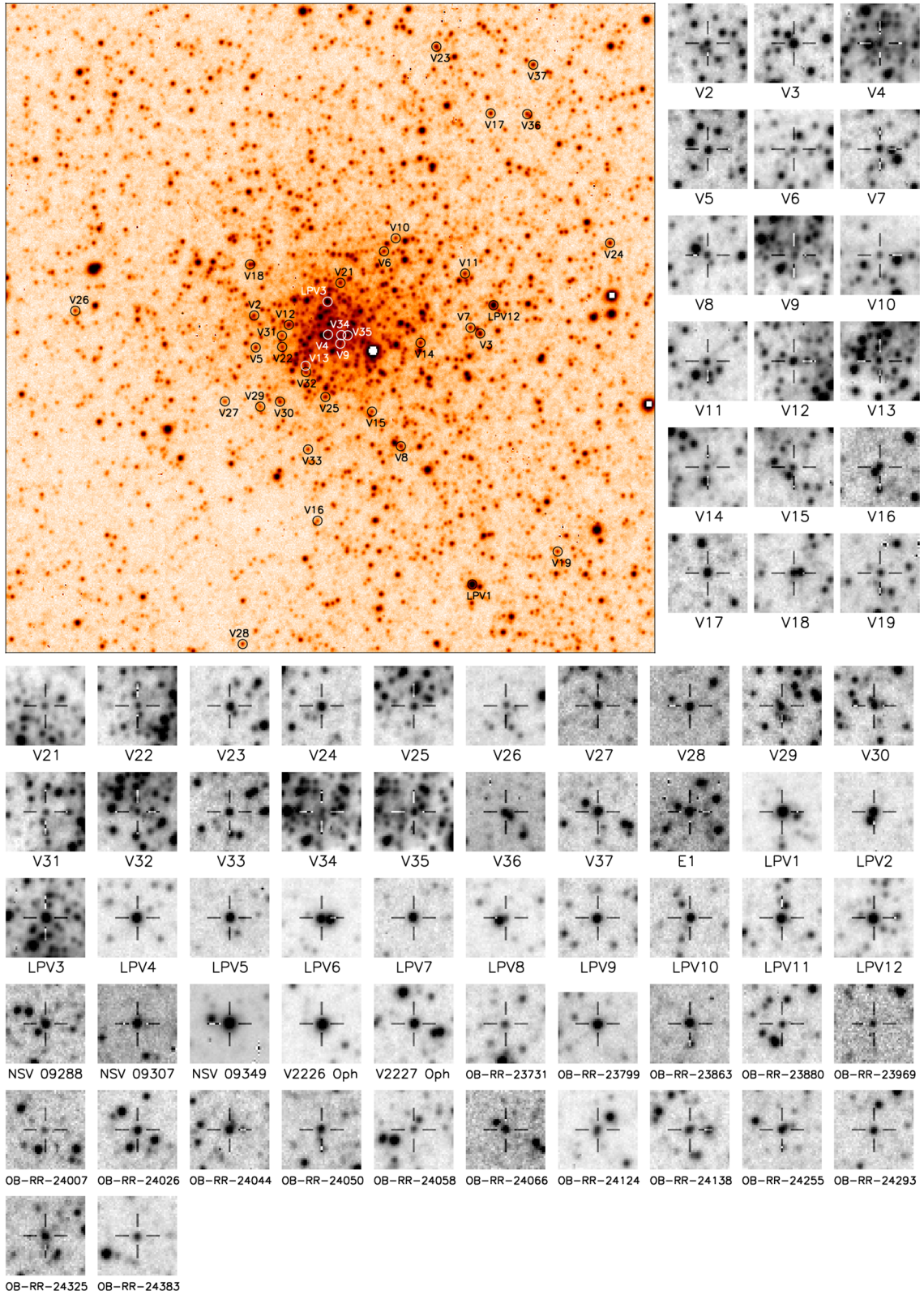
**Figure 4.** Finding chart constructed from our SDSS-$g'$ band reference image covering the cluster region. North is up and East is to the right. The cluster image is $4.8 \times 4.8$ arcmin$^2$. All of the confirmed variables in this sub-field are identified. The image stamps are of size $19.3 \times 19.3$ arcsec$^2$. Each confirmed variable lies at the centre of its corresponding image stamp and is marked by a cross-hair. Image stamps are presented for all confirmed variables in our full FoV. Note that the image stamp for OB-RR-24066 is taken from our SDSS-$i'$ band reference image instead, since it is not detected in the SDSS-$g'$ band reference image. OGLE variable names have been abbreviated for clarity.
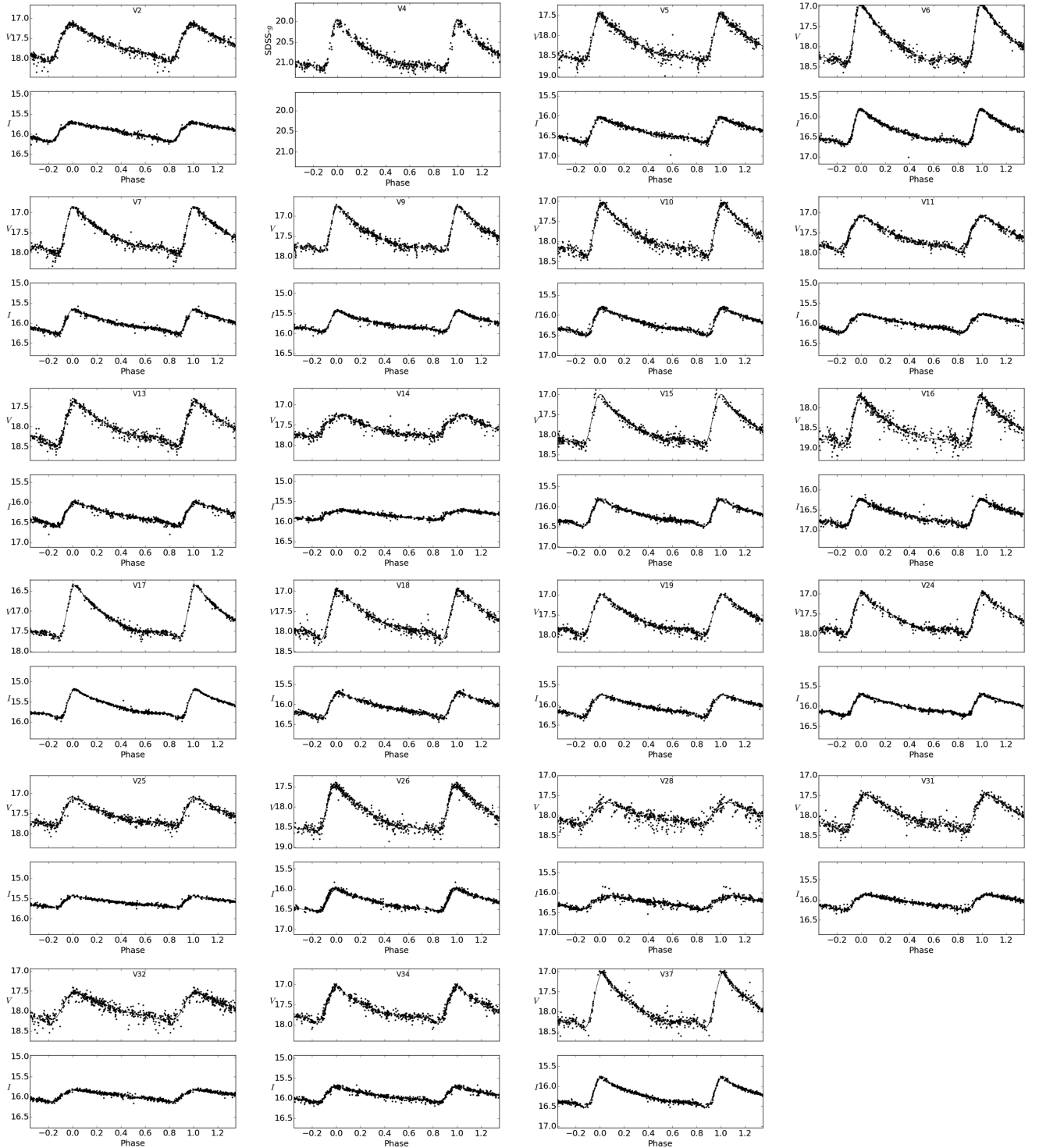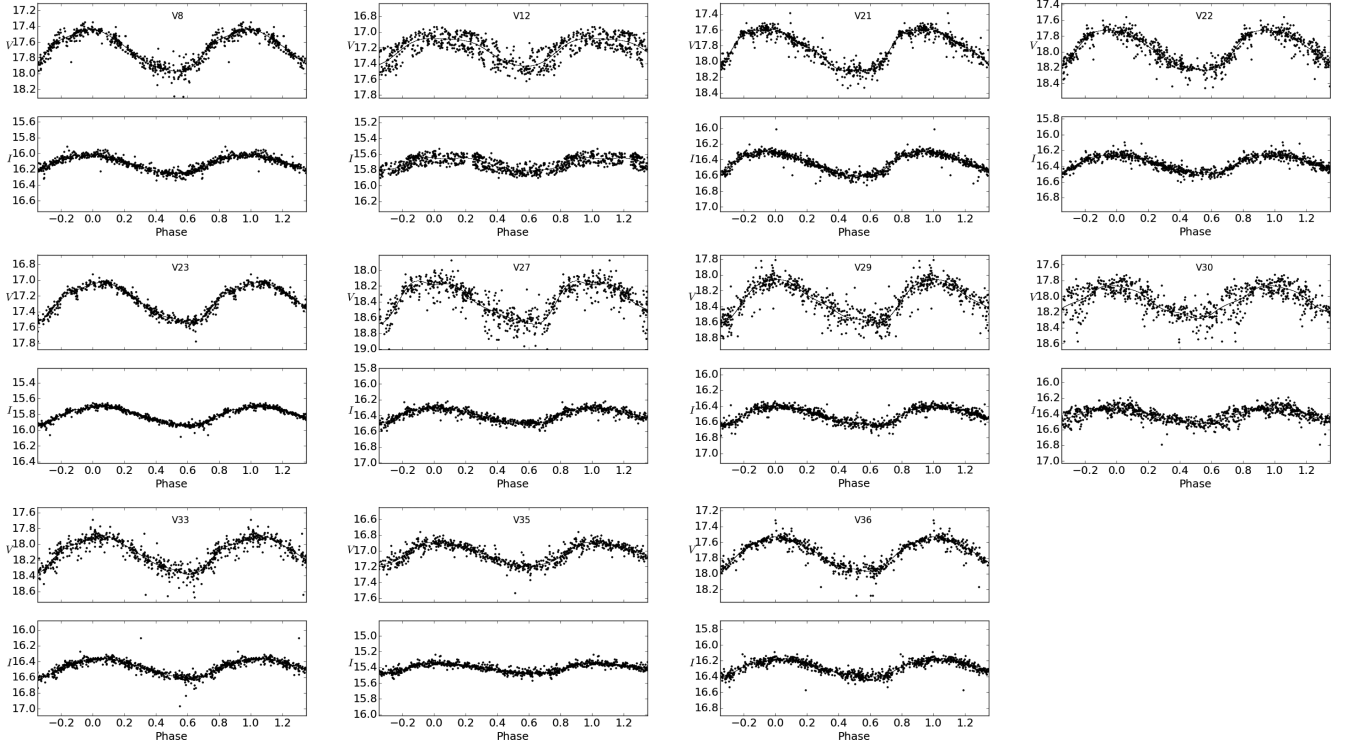
**Figure 5.** Standard SDSS-$g'$ and SDSS-$i'$ band light curves, linearly transformed to the *V* and *I* bands, respectively, for the RRab stars in NGC 6401 phased with the periods listed in Column 5 of Table 3 (or column 4 if no OGLE period was available). Note that no SDSS-$i'$ band data were available for V4 due to its proximity to a bad pixel region on the CCD so only SDSS-$g'$ band instrumental magnitudes are displayed.

exhibits non-radial pulsation (see Section 3.2); V30 shows too much scatter and its Fourier parameters are unreliable; V14 and V28 have a *deviation parameter*, defined by Jurcsik & Kovács (1996), $D_m > 5.0$ and are therefore not suitable to use for calibration purposes. V4 was also not used because it has no SDSS-$i'$ data.

### 4.1 Metallicity

The Fourier decomposition parameters of RRab stars can be used to calculate the metallicity from the semi-empirical relationships of Jurcsik & Kovács (1996), which express [Fe/H] as a function of the period and Fourier parameter $\phi_{31}^{(s)}$, where the superscript *s* denotes

**Figure 6.** Standard SDSS-*g′* and SDSS-*i′* band light curves, linearly transformed to the *V* and *I* bands, respectively, for the RRc stars in NGC 6401 phased with the periods listed in Column 5 of Table 3 (or Column 4 if no OGLE period was available).
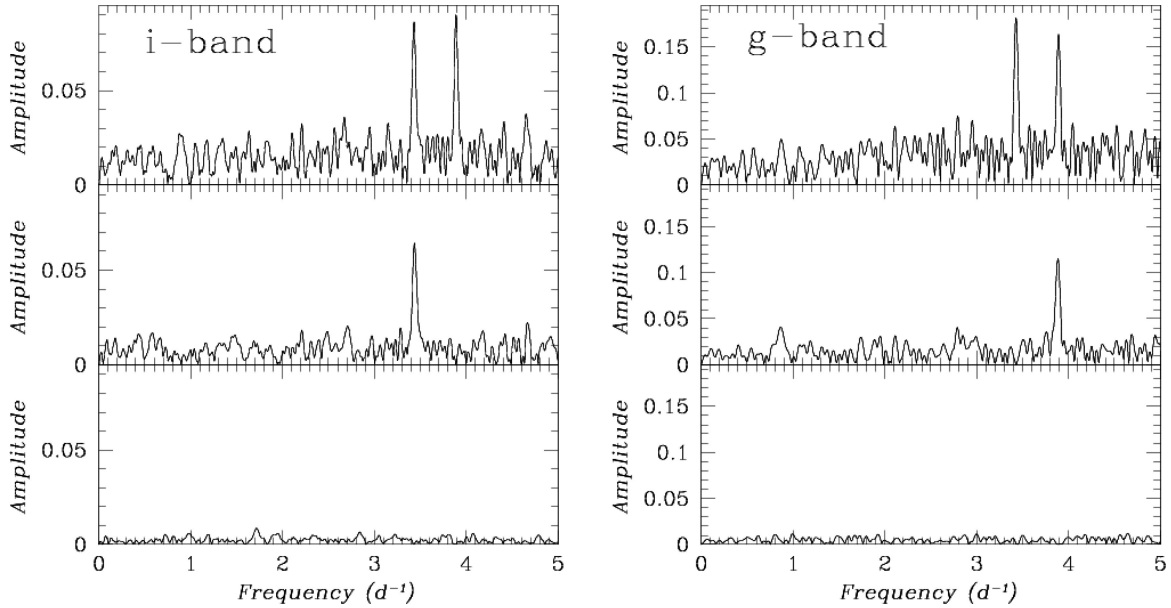


**Figure 7.** Frequency spectra for V12 in the SDSS-*i′* (left) and SDSS-*g′* (right) bands.

a Fourier *sine* series. Since we used a *cosine* series for our fits (6), we converted to *sine* using $\phi_{ij}^{(s)} = \phi_{ij} - (i - j)\frac{\pi}{2}$.

The metallicity is then given by

$$[\text{Fe/H}]_J = -5.038 - 5.394P + 1.345\phi_{31}^{(s)}, \tag{7}$$

where the subscript *J* denotes a non-calibrated metallicity. This can be converted to the metallicity scale of Zinn & West (1984) (hereafter ZW) using the following relationship from Jurcsik (1995):

$$[\text{Fe/H}]_{\text{ZW}} = \frac{[\text{Fe/H}]_J - 0.88}{1.431}. \tag{8}$$

Equation (7) is only applicable to RRab stars with a *deviation parameter* $D_m$ below a given limit. Although Jurcsik & Kovács (1996) originally used $D_m < 3.0$, some authors have relaxed that

**Table 5.** Fourier decomposition parameters (*V* band).

| Star | $A_0$ | $A_1$ | $A_2$ | $A_3$ | $A_4$ | $\phi_{21}$ | $\phi_{31}$ | $\phi_{41}$ | $N$ | $D_m$ |
|------|-------|-------|-------|-------|-------|-------------|-------------|-------------|-----|-------|
| RRab stars | | | | | | | | | | |
| V2  | 17.664 | 0.271 | 0.128 | 0.080 | 0.032 | 4.440 | 9.069 | 7.248 | 6 | 3.14 |
| V5  | 18.234 | 0.323 | 0.160 | 0.111 | 0.065 | 3.953 | 8.313 | 6.350 | 7 | 1.52 |
| V6  | 17.956 | 0.424 | 0.201 | 0.156 | 0.099 | 3.821 | 7.935 | 5.931 | 8 | 3.08 |
| V7  | 17.598 | 0.307 | 0.165 | 0.110 | 0.072 | 3.984 | 8.391 | 6.479 | 8 | 2.39 |
| V9  | 17.510 | 0.289 | 0.142 | 0.109 | 0.070 | 3.950 | 8.089 | 6.053 | 7 | 1.70 |
| V10 | 17.878 | 0.344 | 0.176 | 0.124 | 0.083 | 3.972 | 8.323 | 6.321 | 9 | 2.86 |
| V11 | 17.593 | 0.243 | 0.124 | 0.079 | 0.045 | 4.153 | 8.603 | 6.964 | 6 | 1.13 |
| V13 | 18.037 | 0.292 | 0.163 | 0.105 | 0.064 | 4.102 | 8.596 | 6.779 | 7 | 3.18 |
| V14 | 17.579 | 0.164 | 0.070 | 0.033 | 0.015 | 4.135 | 8.446 | 7.417 | 6 | 7.88 |
| V15 | 17.839 | 0.336 | 0.172 | 0.123 | 0.078 | 3.948 | 8.221 | 6.197 | 6 | 1.81 |
| V16 | 18.508 | 0.320 | 0.166 | 0.117 | 0.088 | 4.006 | 8.282 | 6.327 | 6 | 2.30 |
| V17 | 17.217 | 0.358 | 0.174 | 0.130 | 0.081 | 3.901 | 8.158 | 6.143 | 7 | 1.01 |
| V18 | 17.712 | 0.316 | 0.170 | 0.110 | 0.080 | 4.081 | 8.429 | 6.636 | 6 | 1.94 |
| V19 | 17.625 | 0.282 | 0.147 | 0.097 | 0.060 | 4.065 | 8.495 | 6.692 | 6 | 1.15 |
| V24 | 17.647 | 0.277 | 0.136 | 0.096 | 0.067 | 3.908 | 8.241 | 6.213 | 7 | 2.21 |
| V25 | 17.549 | 0.184 | 0.090 | 0.061 | 0.035 | 4.009 | 8.423 | 6.678 | 7 | 3.41 |
| V26 | 18.216 | 0.335 | 0.150 | 0.103 | 0.065 | 3.936 | 8.229 | 6.051 | 7 | 2.63 |
| V28 | 17.999 | 0.170 | 0.082 | 0.041 | 0.018 | 4.144 | 8.607 | 7.232 | 7 | 5.37 |
| V31 | 18.000 | 0.246 | 0.126 | 0.072 | 0.043 | 4.033 | 8.574 | 6.856 | 6 | 4.73 |
| V32 | 17.941 | 0.201 | 0.094 | 0.047 | 0.020 | 4.328 | 8.983 | 7.103 | 6 | 2.72 |
| V34 | 17.603 | 0.227 | 0.117 | 0.077 | 0.056 | 3.964 | 8.370 | 6.413 | 6 | 2.62 |
| V37 | 17.928 | 0.370 | 0.173 | 0.126 | 0.096 | 3.844 | 8.138 | 6.007 | 6 | 1.89 |
| RRc stars | | | | | | | | | | |
| V8  | 17.707 | 0.205 | 0.015 | 0.013 | 0.007 | 5.002 | 4.222 | 2.888 | 4 | – |
| V12 | 17.234 | 0.144 | 0.024 | 0.012 | 0.001 | 5.968 | 3.033 | 1.745 | 4 | – |
| V21 | 17.861 | 0.226 | 0.035 | 0.015 | 0.020 | 4.758 | 2.985 | 1.830 | 4 | – |
| V22 | 17.983 | 0.202 | 0.026 | 0.015 | 0.009 | 4.586 | 3.359 | 1.670 | 4 | – |
| V23 | 17.279 | 0.196 | 0.015 | 0.016 | 0.010 | 5.029 | 4.357 | 3.074 | 4 | – |
| V27 | 18.404 | 0.195 | 0.037 | 0.030 | 0.013 | 4.689 | 3.543 | 1.477 | 4 | – |
| V29 | 18.344 | 0.205 | 0.039 | 0.015 | 0.014 | 4.408 | 3.193 | 2.263 | 4 | – |
| V30 | 18.074 | 0.156 | 0.007 | 0.008 | 0.011 | 3.731 | 4.977 | 5.157 | 4 | – |
| V33 | 18.131 | 0.185 | 0.018 | 0.016 | 0.010 | 5.075 | 4.747 | 3.342 | 4 | – |
| V35 | 17.048 | 0.117 | 0.015 | 0.008 | 0.005 | 4.808 | 2.378 | 1.185 | 4 | – |
| V36 | 17.756 | 0.174 | 0.016 | 0.012 | 0.009 | 4.477 | 3.908 | 3.005 | 4 | – |

condition to $D_m < 5.0$ with the aim of improving the statistics of the mean physical parameters. We therefore adopted $D_m < 5.0$ as a selection criterion to estimate stellar properties for our RRab stars and have rejected stars V14 and V28 with $D_m > 5.0$ when estimating the physical parameters.

The metallicity can also be obtained for the RRc stars using

$$[\text{Fe/H}]_{\text{ZW}} = 52.466 P^2 - 30.075 P + 0.131\phi_{31}^2 \\ + 0.982\phi_{31} - 4.198\phi_{31} P + 2.424, \quad (9)$$

from Morgan, Wahl & Wieckhorst (2007) (her equation 3).

Metallicity values calculated using these relationships are reported in Tables 6 and 7. The transformation to the UVES (Carretta et al. 2009) scale is given by:

$$[\text{Fe/H}]_{\text{UVES}} = -0.413 + 0.130[\text{Fe/H}]_{\text{ZW}} - 0.356[\text{Fe/H}]_{\text{ZW}}^2. \quad (10)$$

The mean metallicities on the ZW scale for RRab and RRc stars are $-1.254 \pm 0.064$ and $-1.252 \pm 0.210$, respectively.

### 4.2 Effective temperature

The Fourier parameters may also be used to estimate the effective temperature, $T_{\text{eff}}$, for RRab and RRc stars. For the RRab variables,

we used the relationships derived by Jurcsik (1998), which link the $(V - K)_0$ colour to the period $P$:

$$\log(T_{\text{eff}}) = 3.9291 - 0.1112(V - K)_0 - 0.0032[\text{Fe/H}], \quad (11)$$

with

$$(V - K)_0 = 1.585 + 1.257 P - 0.273 A_1 - 0.234\phi_{31}^{(s)} \\ + 0.062\phi_{41}^{(s)}. \quad (12)$$

For the RRc stars the calibration of Simon & Clement (1993) can be used:

$$\log(T_{\text{eff}}) = 3.7746 - 0.1452 \log(P) + 0.0056\phi_{31}. \quad (13)$$

Note that the temperatures for RRab and RRc stars calculated using the relationships above are on different absolute scales. For a discussion on the accuracy and caveats of these calibrations we refer the reader to Cacciari, Corwin & Carney (2005), Arellano Ferro et al. (2008) and Bramich et al. (2011).

The mean effective temperature for the RRab stars is $6503.87 \pm 78.37$ K and for the RRc stars $7397.68 \pm 49.23$ K.

**Table 6.** Physical parameters for the RRab stars in NGC 6401. Stars marked with an asterisk (*) were not included when estimating averages. Column 6 lists the reddening calculated using the minimum light method, while Column 7 lists the values obtained using equation (19).

| Star | $[Fe/H]_{ZW}$ | $M_V$ | $\log(L/L_\odot)$ | $T_{eff}$ | $E(V-I)$ | $E(V-I)$ [KW01] | Distance (kpc) |
|------|------|------|------|------|------|------|------|
| | | | RRab stars | | | | |
| V2 | −1.212 | 0.450 | 1.725 | 6344.22 | 1.292 | 1.339 | 6.406 |
| V5 | −1.287 | 0.638 | 1.651 | 6522.05 | 1.405 | 1.491 | 6.720 |
| V6 | −1.305 | 0.708 | 1.624 | 6654.18 | 1.176 | 1.305 | 7.419 |
| V7 | −1.258 | 0.639 | 1.651 | 6504.83 | 1.146 | 1.224 | 6.726 |
| V9 | −1.419 | 0.709 | 1.627 | 6502.29 | 1.344 | 1.422 | 4.993 |
| V10 | −1.248 | 0.637 | 1.651 | 6552.30 | 1.249 | 1.340 | 6.808 |
| V11 | −1.196 | 0.634 | 1.651 | 6429.07 | 1.114 | 1.171 | 6.970 |
| V13 | −1.140 | 0.623 | 1.654 | 6498.34 | 1.257 | 1.327 | 7.306 |
| V14* | −1.444 | 0.652 | 1.650 | 6250.92 | 1.248 | 1.286 | 5.899 |
| V15 | −1.270 | 0.676 | 1.636 | 6564.51 | 1.210 | 1.302 | 6.866 |
| V16 | −1.210 | 0.692 | 1.628 | 6565.09 | 1.424 | 1.512 | 7.278 |
| V17 | −1.325 | 0.659 | 1.644 | 6561.62 | 1.177 | 1.276 | 5.396 |
| V18 | −1.315 | 0.592 | 1.671 | 6460.35 | 1.218 | 1.294 | 6.670 |
| V19 | −1.213 | 0.636 | 1.651 | 6480.19 | 1.126 | 1.196 | 6.972 |
| V24 | −1.303 | 0.701 | 1.627 | 6517.09 | 1.183 | 1.259 | 6.407 |
| V25 | −1.277 | 0.722 | 1.618 | 6415.69 | 1.486 | 1.531 | 4.302 |
| V26 | −1.227 | 0.676 | 1.635 | 6599.57 | 1.469 | 1.570 | 6.088 |
| V28* | −1.350 | 0.631 | 1.656 | 6295.70 | 1.249 | 1.284 | 7.219 |
| V31 | −1.210 | 0.631 | 1.653 | 6438.13 | 1.487 | 1.548 | 5.516 |
| V32 | −1.135 | 0.554 | 1.682 | 6375.44 | 1.508 | 1.546 | 5.430 |
| V34 | −1.277 | 0.704 | 1.625 | 6469.60 | 1.204 | 1.263 | 6.121 |
| V37 | −1.247 | 0.684 | 1.633 | 6622.74 | 1.269 | 1.379 | 6.667 |
| Weighted | −1.254 | 0.648 | 1.647 | 6503.87 | 1.287 | 1.365 | 6.353 |
| Mean | ± 0.064 | ± 0.062 | ± 0.024 | ± 78.37 | ± 0.128 | ± 0.124 | ± 0.814 |

**Table 7.** Physical parameters for the RRc stars in NGC 6401. Stars marked with an asterisk (*) were not included when estimating averages.

| Star | $[Fe/H]_{ZW}$ | $M_V$ | $\log(L/L_\odot)$ | $T_{eff}$ |
|------|------|------|------|------|
| | | RRc stars | | |
| V8 | −1.086 | 0.566 | 1.676 | 7398.51 |
| V12* | −1.408 | 0.584 | 1.676 | 7403.00 |
| V21 | −1.269 | 0.566 | 1.680 | 7447.49 |
| V22 | −1.327 | 0.600 | 1.668 | 7402.74 |
| V23 | −1.489 | 0.514 | 1.706 | 7282.88 |
| V27 | −1.043 | 0.588 | 1.666 | 7464.05 |
| V29 | −1.282 | 0.598 | 1.668 | 7427.72 |
| V30* | 0.802 | 0.663 | 1.592 | 7707.52 |
| V33 | −0.911 | 0.536 | 1.683 | 7396.88 |
| V35 | −1.635 | 0.626 | 1.665 | 7370.81 |
| V36 | −1.226 | 0.587 | 1.671 | 7388.00 |
| Weighted | −1.252 | 0.576 | 1.676 | 7397.68 |
| Mean | ± 0.210 | ± 0.032 | ± 0.012 | ± 49.23 |

### 4.3 Absolute magnitudes

For the RRab stars, we used Kovacs & Walker (2001) to derive the absolute magnitude

$$M_V = -1.876 \log P - 1.158A_1 + 0.821A_3 + K_0, \tag{14}$$

where the zero-point of the calibration is $K_0 = 0.41 \pm 0.02$ mag, as discussed in Kains et al. (2015).

For the RRc stars, equation (10) from Kovacs (1998) is used instead, after adopting the zero-point value $K_1 = 1.061 \pm 0.02$ mag used in Cacciari et al. (2005):

$$M_V = K_1 - 0.961P - 0.044\phi_{21}^{(s)} - 4.447A_4. \tag{15}$$
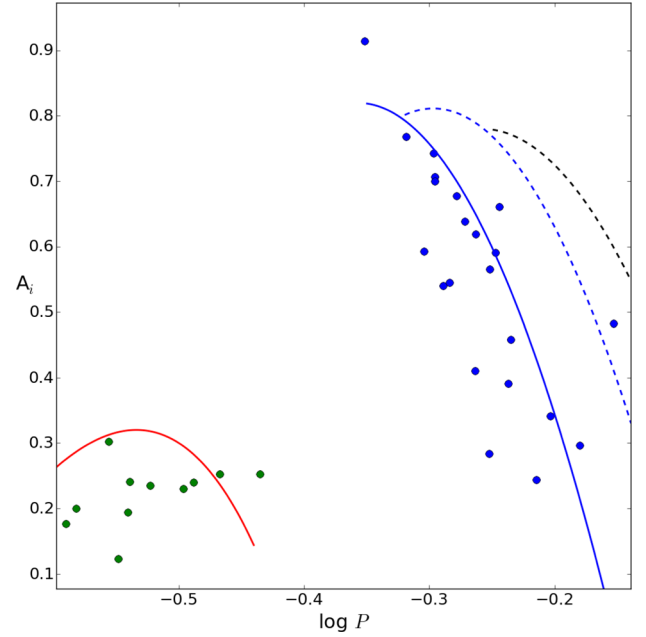
**Figure 8.** Period–amplitude distributions for the RR Lyrae stars in NGC 6401 in the SDSS-*i'* band. RRab and RRc stars are marked with blue and green circles, respectively. The dashed black curve was calculated by Arellano Ferro et al. (2011, 2013) for the OoII clusters NGC 5024 and NGC 6333. The solid blue and dashed blue curves are from Kunder et al. (2013) for the OoI cluster NGC 2808 and correspond to the mean distributions of regular and evolved stars, respectively. The red curve was calculated by Arellano Ferro et al. (2015) for a sample of RRc stars in five OoI type clusters.

The magnitudes were then converted to luminosities using

$$\log(L/L_\odot) = -0.4(M_V - M_{bol,\odot} + B_C) \tag{16}$$

where $M_{bol,\odot} = 4.75$ is the solar bolometric magnitude and $B_C = 0.06[Fe/H]_{ZW} + 0.06$ is the bolometric correction term given by Sandage & Cacciari (1990).

The mean absolute magnitudes for the RRab and RRc stars are $0.648 \pm 0.062$ and $0.576 \pm 0.032$, respectively.

### 4.4 Bailey diagram and Oosterhoff type

We could not find any assessment of the Oosterhoff type of NGC 6401 in the literature. Using the RR Lyrae variable stars listed in Table 3, we estimated mean periods $\langle P_{RRab} \rangle = 0.55 \pm 0.06$ d and $\langle P_{RRc} \rangle = 0.30 \pm 0.03$ d. We found that 68 per cent of the RR Lyrae variables in the cluster are RRab's. These values and the derived metallicity of NGC 6401 indicate that the cluster is Oosterhoff type I (e.g. Clement et al. 2001).

The SDSS-*i'* band Bailey diagram ($\log P$ versus $A_i$) for the cluster RR Lyrae variables is shown in Fig. 8. Since RRab stars have longer periods and greater amplitudes than RRc stars, they occupy distinctly different areas in the figure. Solid and dashed lines mark the mean distributions of regular and evolved stars for Oosterhoff type I (OoI) and type II (OoII) clusters. The proximity of the NGC 6401 RRab and RRc locations to the lines corresponding to OoI clusters confirms our classification. We do not present the corresponding SDSS-*g'* band diagram since we have no comparison theoretical lines to display.

### 4.5 Correcting for extinction

As pointed out in Barbuy et al. (1999), NGC 6401 suffers from heavy differential reddening. Foreground reddening estimates at and around the cluster centre coordinates range from $E(B − V) = 0.53$ (Barbuy et al. 1999) to $E(B − V) = 1.1$ (Valenti et al. 2007), with multiple authors giving estimates in between those extremes [e.g. $E(B − V) = 0.85$, Harris 1996; Piotto et al. 2002; 0.81, Bica & Allain 1986; Schlafly & Finkbeiner 2011; 0.59, Minniti 1995b; 0.96, Schlegel, Finkbeiner & Davis 1998. These can be converted to $E(V − I)$ reddening values through $E(V − I) = 1.259E(B − V)$, derived from Schlegel et al. (1998). In order to derive reasonable distances to the cluster, appropriate reddening calibrations need to be applied.

After taking into account small corrections for period and metallicity differences between stars, Sturch (1966) discovered that all RRab stars have nearly the same dereddened $(B − V)$ colour at minimum light (i.e. between the phase interval 0.5 and 0.8). Mateo et al. (1995) suggested that $(V − I)$ colour at minimum light is a better indicator of foreground reddening. This was confirmed by Day et al. (2002), who found that the mean dereddened $(V − I)$ colour at minimum light was $0.57 ± 0.025$ mag, with little-to-no dependence on metallicity or period. This was further refined by Guldenschuh et al. (2005) to $\overline{(V − I)}_{0,\min} = 0.58 ± 0.02$ mag, who also found no dependence on metallicity or pulsation amplitude. Guldenschuh also provided an independent colour–metallicity calibration in the form of $\overline{(V − I)}_{0,\min} = 0.569 − 0.008[\text{Fe/H}]$, with an rms of 0.024 mag. Kunder & Chaboyer (2010) validated these relationships for RRab stars in the Galactic bulge.

To determine distances to individual RRab stars, we calculated the mean dereddened magnitudes using $I_0 = I − A_I$ and $V_0 = V − A_V$. The value for the extinction $A_I$ was obtained using the relationships in Schlegel et al. (1998):

$$A_I = 1.4626E(V − I), \tag{17}$$

and, again following Schlegel et al. (1998), $A_V = 1.6835A_I$. The reddening in the optical is given by

$$E(V − I) = (V − I) − (V − I)_0, \tag{18}$$

where the colour $(V − I)$ is evaluated from the observed RRab colour at minimum light, and $(V − I)_0$ is the intrinsic colour at minimum light $\overline{(V − I)}_{0,\min} = 0.58$ mag. For comparison, we also provide the reddening values obtained using the following approximate formula from Kovacs & Walker (2001):

$$(V − I)_0 = 0.253\log(P) − 0.388A_1 + 0.364A_3 + 0.648. \tag{19}$$

The reddening values evaluated using the minimum light method are given in Column 6 of Table 6 and those calculated via expression (19) in Column 7.

### 4.6 Distance to NGC 6401 using RR Lyrae stars

The absolute magnitude $M_V$ can be used to determine the distance $d$ to each RRab star using:

$$d = 10^{1+0.2(V_0 − M_V)}, \tag{20}$$

where $V_0$ is the star's dereddened magnitude. We obtain a mean distance to the cluster $d ≈ 6.35 ± 0.81$ kpc. The derived distance is consistent with the value reported in Valenti et al. (2007) ($d ≈ 7.7$ kpc) and significantly lower than the one found by Barbuy et al. (1999) ($d ≈ 12.0 ± 1.0$ kpc). Our distances were estimated using the intrinsic colour at minimum light method.

## 5 DISCUSSION

This work presents the first detailed photometric time series study of NGC 6401 employing CCD data. NGC 6401 is a little-investigated globular cluster 5°3 from the Galactic Centre. It is affected by strong differential reddening, which complicates photometric calibration, and hence the estimation of the physical parameters. This is possibly one of the reasons it has not been extensively studied in the past.

Using the RR Lyrae stars that are the most plausible cluster members, we have determined that NGC 6401 is an OoI cluster of intermediate metallicity that belongs to the metal-rich population of ∼20 bulge clusters that lie within 2 kpc from the Galactic Centre (Minniti 1995a). Bica, Ortolani & Barbuy (2016) conclude that a cut-off of 3 kpc from the Galactic Centre is suitable in terms of isolating a bona-fide bulge cluster sample, with little contamination. As pointed out by Rossi et al. (2015), inner bulge globular clusters appear to be trapped in the bulge bar due to its high mass. This is very likely the case for NGC 6401 as well, since it is also in the bulge (Zoccali & Valenti 2016).

Forbes & Forte (2001) argue that the mean metallicity of globular clusters reveals information about the mass of the host galaxy because the chemical enrichment of globular clusters is directly linked to the galaxy formation process. In particular, they claim that the inner metal-rich globular clusters and the bulge field stars have similar colours because they formed at the same time from the same chemically enriched gas. Their findings agree with those of Barbuy, Bica & Ortolani (1998), who also conclude that bulge clusters share comparable properties with the bulge field stars, including not only metal-rich globular clusters, but also intermediate metallicity ones. In this work, we have derived independent metallicity and distance estimates for NGC 6401, which are compatible with the characteristics of other metal-rich globular clusters in the Galactic bulge. Our results provide further support to the idea that the bulge field stars and the inner globular cluster population evolved on the same time-scales.

## 6 SUMMARY

We have updated the census of variable stars in NGC 6401. We use three different methods to recover 34 RR Lyrae cluster variables, three of which do not appear in the OGLE data base (V8, V10 and V14). We do not find evidence of variability for the previously reported variables V1, V20 and OGLE-BLG-RRLYR-23724. We discovered 13 new variables, E1 and LPV1–12 and classified V3 as a W Virginis star for the first time. We detected double-mode non-radial pulsations in the RRc star V12, adding another example of these rare objects in globular clusters. Finally, we used the RR Lyrae content to establish that NGC6401 is an OoI type cluster.

The parameters obtained through Fourier decomposition of the light curves of a selected subset of RRab and RRc stars were used to estimate the metallicity, absolute magnitude, luminosity and effective temperature of each variable. The average metallicity for the cluster derived using the RRab stars $[\text{Fe/H}]_{\text{ZW}} = −1.25 ± 0.06$ ($[\text{Fe/H}]_{\text{UVES}} = −1.13 ± 0.06$) is consistent with that evaluated from the RRc stars $[\text{Fe/H}]_{\text{ZW}} = −1.25 ± 0.21$ and lower than the estimate by Barbuy et al. (1999).

The mean distance to the cluster, estimated after individual RRab stars were corrected for differential reddening, is $d ≈ 6.35 ± 0.81$ kpc.

## REFERENCES

Alard C., Lupton R. H., 1998, ApJ, 503, 325
Alcock C. et al., 2000, ApJ, 542, 257
Arellano Ferro A., Rojas Lopez V., Giridhar S., Bramich D. M., 2008, MNRAS, 384, 1444
Arellano Ferro A., Figuera Jaimes R., Giridhar S., Bramich D. M., Hernandez Santisteban J. V., Kuppuswamy K., 2011, MNRAS, 416, 2265
Arellano Ferro A. et al., 2013, MNRAS, 434, 1220
Arellano Ferro A., Mancera Piña P. E., Bramich D. M., Giridhar S., Ahumada J. A., Kains N., Kuppuswamy K., 2015, MNRAS, 452, 727
Barbuy B., Bica E., Ortolani S., 1998, A&A, 333, 117
Barbuy B., Ortolani S., Bica E., Desidera S., 1999, A&A, 348, 783
Bica E., Allain D., 1986, A&AS, 66, 171
Bica1 E., Ortolani E., Barbuy B., 2016, PASA, 33, e028
Blu T., Thevenaz P., Unser M., 2001, IEEE Trans. Image Process., 10, 1069
Bramich D. M., 2008, MNRAS, 386, L77
Bramich D. M., Freudling W., 2012, MNRAS, 424, 1584
Bramich D. M., Figuera Jaimes R., Giridhar S., Arellano Ferro A., 2011, MNRAS, 413, 1275
Bramich D. M. et al., 2013, MNRAS, 428, 2275
Bramich D. M., Bachelet E., Alsubai K. A., Mislis D., Parley N., 2015, A&A, 577, 108
Cacciari C., Corwin T. M., Carney B. W., 2005, AJ, 129, 267
Cardelli J. A., Clayton G. C., Mathis J. S., 1989, ApJ, 345, 245
Carretta E., Bragaglia A., Gratton R., D'Orazi V., Lucatello S., 2009, A&A, 508, 695
Clement C. M. et al., 2001, AJ, 122, 2587
Davidge T. J., 2001, AJ, 121, 3100
Day A. S. et al., 2002, PASP, 114, 645
Draper P. W., 2000, in Manset N., Veillet C., Crabtree D., eds, ASP Conf. Ser. Vol. 216, Astronomical Data Analysis Software and Systems IX. Astron. Soc. Pac., San Francisco, p. 615
Figuera Jaimes R., Arellano Ferro A., Bramich D. M., Giridhar S., Kuppuswamy K., 2013, A&A, 556, 20
Forbes D. A., Forte J. C., 2001, MNRAS, 322, 257
Guldenschuh K. A. et al., 2005, PASP, 117, 721
Harris W. E., 1996, AJ, 112, 1487
Ivezic Z. et al., 2007, AJ, 134, 973
Jurcsik J., 1995, Act. Astron., 45, 653
Jurcsik J., 1998, A&A, 333, 571
Jurcsik J., Kovács G., 1996, A&A, 312, 111
Kains N. et al., 2015, A&A, 578, 128
Kovács G., 1998, MmSAI, 69, 49

Kovács G., Walker A. R., 2001, A&A 371, 579
Kunder A., Chaboyer B., 2010, AJ, 139, 415
Kunder A. et al., 2013, AJ, 146, 119
Lupton R., 2005, http://classic.sdss.org/dr4/algorithms/sdssUBVRITransform.html
Mateo M., Udalski A., Szymanski M., Kaluzny J., Kubiak M., Krzeminski W., 1995, AJ, 109, 588
Minniti D., 1995a, AJ, 109, 4
Minniti D., 1995b, A&A, 303, 468
Morgan S. M., Wahl J. N., Wieckhorst R. M., 2007, MNRAS, 374, 1421
Olech A., Kaluzny J., Thompson I. B., Pych W., Krzeminski W., Schwarzenberg-Czerny A., 1999, ApJ, 118, 452
Pal A., Bakos G. A., 2006, PSP, 118, 1474
Piotto G. et al., 2002, A&A, 391, 945
Rossi L. J., Ortolani S., Barbuy B., Bica E., Bonfanti A., 2015, MNRAS, 450, 3270
Samus N. N., Kazarovets E. V., Pastukhova E. N., Tsvetkova T. M., Durlevich O. V., 2009a, PASP, 121, 1378
Samus N. N., Goranskij V. P., Durlevich O. V., Kazarovets E. V., Kireeva N. N., Pastukhova E. N., Zharova A. V., 2009b, VizieR Online Data Catalog, 1, 2025
Sandage A., Cacciari C., 1990, ApJ, 350, 645
Schlafly E. F., Finkbeiner D. P., 2011, ApJ, 737, 103
Schlegel D. J., Finkbeiner D. P., Davis M., 1998, ApJ, 500, 525
Simon N. R., Clement C. M., 1993, ApJ, 410, 526
Soszynski I. et al., 2014, Acta Astron., 64, 177
Stetson P. B., 1987, PASP, 99, 191
Sturch C., 1966, ApJ, 143, 774
Terzan A., Rutily B., 1972, A&A, 16, 408
Terzan A., Rutily B., 1973, IAU Colloq. 21: Variable Stars in Globular Clusters and in Related Systems. Reidel Publishers, p. 68
Terzan A., Rutily B., 1975, A&A, 38, 307
Tsapras Y. et al., 2009, Astron. Nachr., 330, 4
Udalski A., 2003, Acta Astron., 53, 291
Udalski A., Szymanski M. K., Szymanski G., 2015, Acta Astron., 65, 1
Valenti E., Ferraro F. R., Origlia L., 2007, AJ, 133, 1287
Zacharias N., Finch C. T., Girard T. M., Henden A., Bartlett J. L., Monet D. G., Zacharias M. I., 2012, AJ, 145, 44
West, M. J., Zinn R., 1984, ApJS, 55, 45 (ZW)
Zoccali M., Valenti E., 2016, PASA, 33, 25

## SUPPORTING INFORMATION

Supplementary data are available at *MNRAS* online.

**Table 2.** Time-series SDSS-$g'$ and SDSS-$i'$ photometry, linearly transformed to the *V* and *I* bands, respectively, for all of the confirmed variables in our field of view.

Please note: Oxford University Press is not responsible for the content or functionality of any supporting materials supplied by the authors. Any queries (other than missing material) should be directed to the corresponding author for the article.

## APPENDIX A: SUPPLEMENTARY LIGHT CURVES
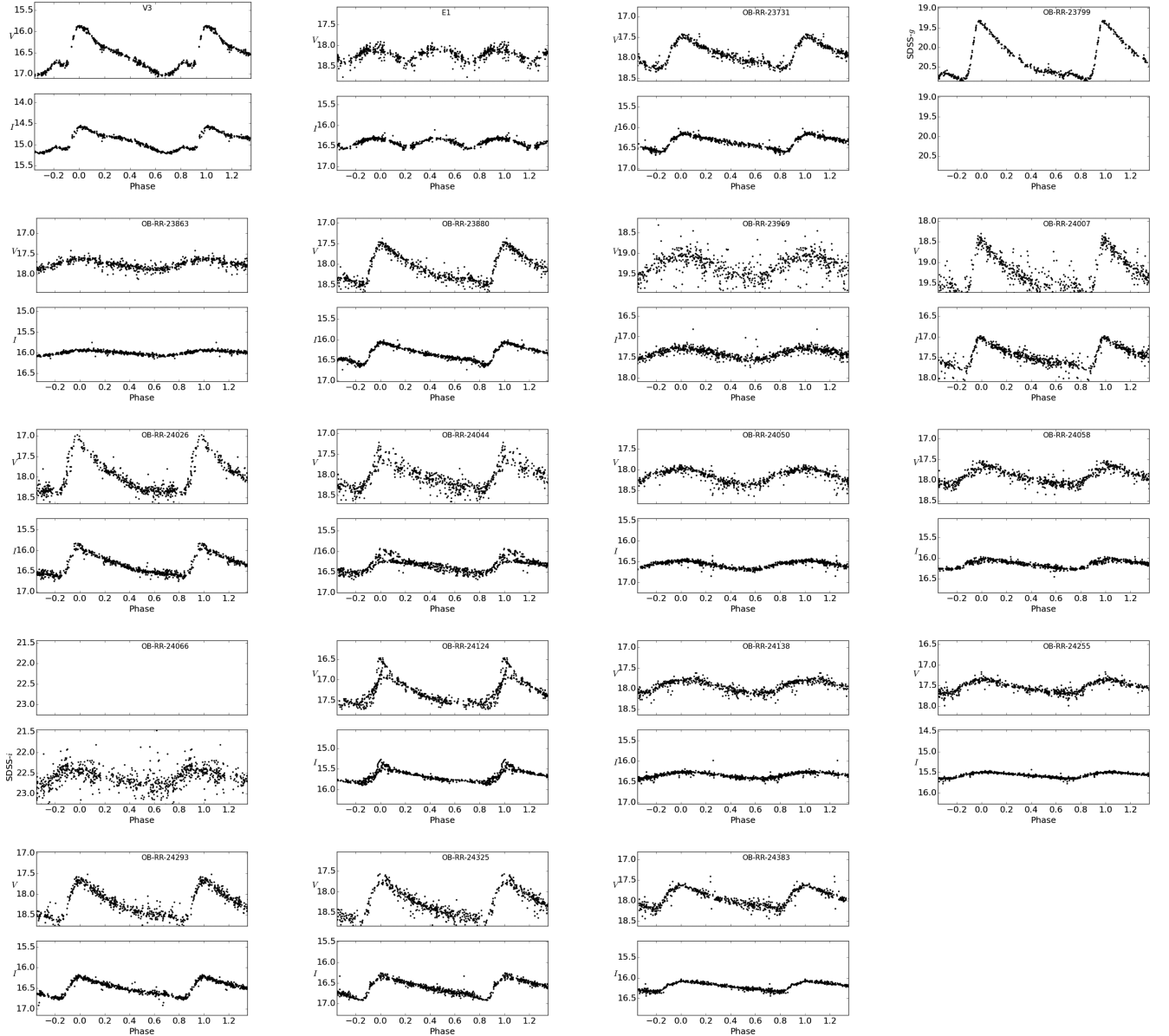


**Figure A1.** Standard SDSS-$g'$ and SDSS-$i'$ band light curves, linearly transformed to the $V$ and $I$ bands, respectively, for V3, E1 and the RR Lyrae variable stars listed in Table 4. Note that no SDSS-$i'$ band data were available for OB-RR-23799 so only SDSS-$g'$ band instrumental magnitudes are displayed, and vice versa for OB-RR-24066.
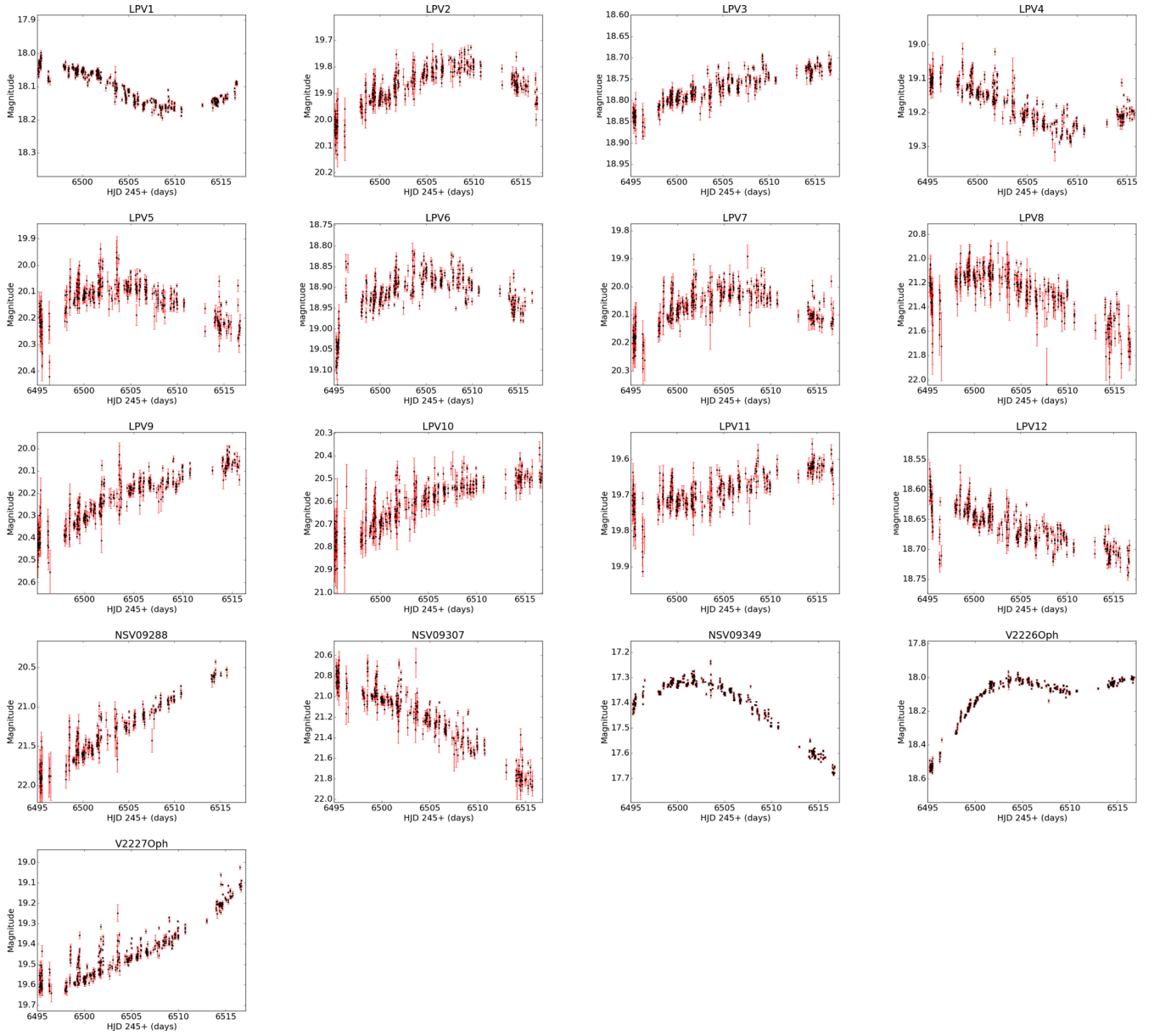
**Figure A2.** Light curves of the LPV stars listed in Table 4. The reported magnitudes are in the instrumental SDSS-*g'* scale.

This paper has been typeset from a TEX/LATEX file prepared by the author.